



Investigation on the Creep Behavior of AZ91 Magnesium Alloy Processed by Severe Plastic Deformation

Iraj Khoubrou¹ · Bahram Nami¹ · Seyyed Mehdi Miresmaeili¹

Received: 13 March 2019 / Accepted: 31 May 2019 / Published online: 11 June 2019
© The Korean Institute of Metals and Materials 2019

Abstract

This paper describes the grain refinement due to equal-channel angular pressing (ECAP) and the creep properties of the ECAP-processed AZ91 magnesium alloy. The resulting microstructure and creep properties were examined by scanning electron microscope and impression creep test method. Microstructural evolution reveals that the grains were refined to 14 μm after four ECAP passes at 628 K, following route Bc. The creep tests were carried out under stresses in the range of 35 to 95 MPa at temperatures in the range of 538 to 583 K. Based on a power law between the impression rate and stress, the stress exponents were about 2 and the activation energies were about 129 kJ/mol, which are close to that for lattice diffusion of magnesium. Considering the obtained results, it can be stated that the grain boundary sliding is the dominant creep mechanism at low stresses and high temperatures.

Keywords Magnesium alloy · Equal-channel angular pressing · Creep properties · Grain boundary sliding · Microstructure

1 Introduction

Magnesium alloys are widely used in various industries and engineering applications. Their special properties including high specific strength and low density make them attractive to industries such as automobile, aircraft, and electronics [1–5]. Among the magnesium alloys, AZ series alloys such as AZ91 is the most common commercial magnesium alloy, which has the good features such as suitable mechanical properties at ambient temperature, good corrosion resistance, and superior castability [6, 7]. However, Magnesium alloys have poor workability and limited ductility, because their crystal structure is hexagonal close packed (hcp) with limited slip systems [8–10]. In some cases, the parts used in the industry require suitable formability that will not be by the casting process. Microstructural refinement usually

leads to increase both strength and ductility of magnesium and its alloys. Ultrafine-grained (UFG) microstructures can be produced by severe plastic deformation (SPD) techniques in the sub-micrometer to nanometer range for bulk metallic material. Among all SPD techniques, equal-channel angular pressing (ECAP) is the most effective method in which a sample is pressed in a die containing two channels with the same cross-section [11–14]. High temperature deformation behavior of UFG magnesium alloy has been reported in previous studies [15–21]. It has been shown that the grain boundary sliding is the controlling deformation mechanism during deformation of AZ91, AZ31, ZK60, ZK40, and ZK30 alloys at elevated temperatures [15–21].

Impression creep has been used frequently in the literature so far. According to the published paper in all of the researches, the obtained creep mechanisms were dislocation creep on the Mg alloys. The other deformation mechanisms during creep of the Mg alloys have not been studied using impression creep method. So, the aim of this study was the capability of impression creep method in investigating grain boundary sliding mechanism. For this purpose, it is needed to have a microstructure with fine and almost uniform grain size. Results of previous studies indicated that a microstructure with those characteristics can be obtained using at least four ECAP passes method. So, in the current study, the effect of microstructural evolution during processing by

✉ Bahram Nami
bnami@sru.ac.ir

Iraj Khoubrou
i.khoubrou@yahoo.com

Seyyed Mehdi Miresmaeili
s.m.miresmaeili@sru.ac.ir

¹ Department of Materials Engineering and New Technologies, Shahid Rajaei Teacher Training University (SRTTU), Lavizan, Tehran, Iran

four ECAP passes on the creep properties and deformation behavior at the elevated temperature of AZ91 magnesium alloy have been investigated.

2 Materials and Methods

The alloy used in the present study was a commercial AZ91 magnesium alloy containing 8.9 wt% Al, 0.9 wt% Zn and 0.21 wt% Mn. This alloy was prepared from high purity Magnesium (99.95 wt%), Aluminum (99.8 wt%) and Zinc (99.9 wt%) ingots using the casting process. Melting was carried out in a cylindrical electric resistance furnace with a graphite crucible under Ar gas atmosphere to protect melt from oxidation. After melting Mg at 1023 K, Al, Zn, and pure Mn flakes were added as alloying elements to the melt. The melt was kept at this temperature for 20 min and mechanically stirred for 2 min by a stainless steel rod in order to obtain a uniform chemical composition. Before pouring the melt, the steel mold with $140 \times 55 \times 12$ mm dimensions was preheated up to 523 K. Finally, the melt was poured in the mold using a tilt casting technique. ECAP experiments were conducted using a solid die with an angle of 90° between the two channels (Φ) and external angle (Ψ) of 20° as shown in Fig. 1. The ECAP billets having a dimension of $12 \times 12 \times 100$ mm were machined from the as-cast alloy. The billets and die channels were sprayed with molybdenum disulfide (MoS_2) lubricant to minimize the friction effect. The die was heated to the testing temperature and ECAP specimen was held at the die for 20 min before pressing. The ECA pressing carried out at a temperature of 628 ± 3 K with the pressing speed of 0.2 mm/s for four passes and processing route Bc was used. Creep specimens with a dimension of $12 \times 12 \times 15$ mm were prepared from

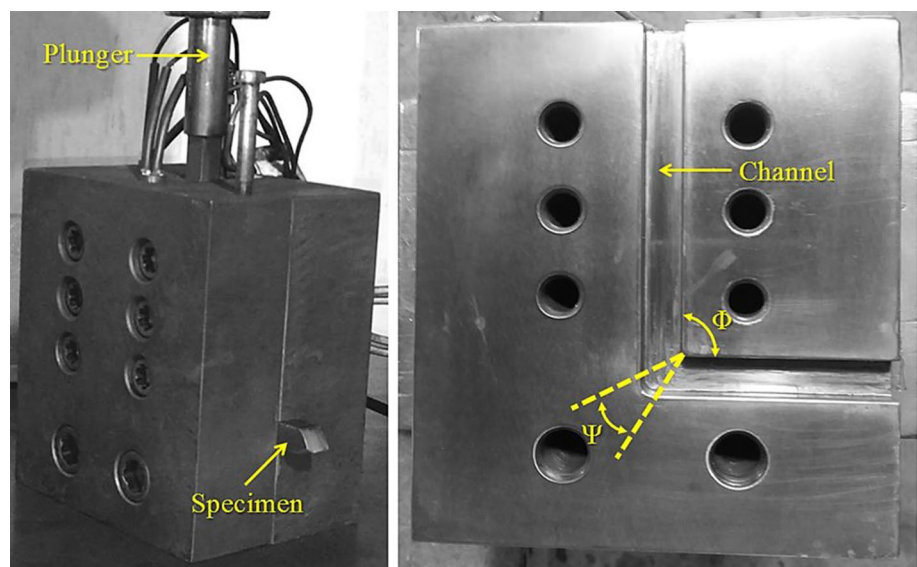
the ECAPed specimens. The creep tests were performed at the temperature range of 538–583 K under shear modulus normalized stress between 0.00256 and 0.00694 using impression method. The impression depth with a resolution of ± 1 μm was recorded during the dwell time using a flat-ended cylindrical punch with 2.5 mm diameter. The as-cast and ECAPed microstructure, as well as the evolution of microstructure after creep, were examined by scanning electron microscope (SEM). The samples were prepared by standard grinding and polishing methods and etched with an acetic picric etchant (5 ml acetic acid, 6 g picric acid, 10 ml H_2O and 100 ml ethanol) at room temperature.

3 Results and Discussion

3.1 Microstructure

Figure 2 shows the scanning electron microscope images of the as-cast AZ91 alloy. According to this figure, it can be seen that the microstructure of the AZ91 alloy consists of $\alpha(\text{Mg})$ matrix phase and intermetallic compound. XRD investigation of AZ91 alloy in our previous studies [22] indicates that $\beta(\text{Mg}_{17}\text{Al}_{12})$ is the sole intermetallic compounds composed in the alloy microstructure. The $\beta(\text{Mg}_{17}\text{Al}_{12})$ phase has been distributed mainly in the grain boundaries with massive (point A) and lamellar (point B) morphology. Massive and lamellar $\beta(\text{Mg}_{17}\text{Al}_{12})$ phases formed during alloy cooling process due to the decreasing Al solubility and eutectic reaction, respectively. Similar microstructural features have been reported for as-cast AZ91 alloy in previous studies [22, 23]. The scanning electron microscope images of AZ91 alloy after ECAP processing are shown in Fig. 3. It can be seen that the grains are almost equiaxed with sharp

Fig. 1 ECAP die used in this study



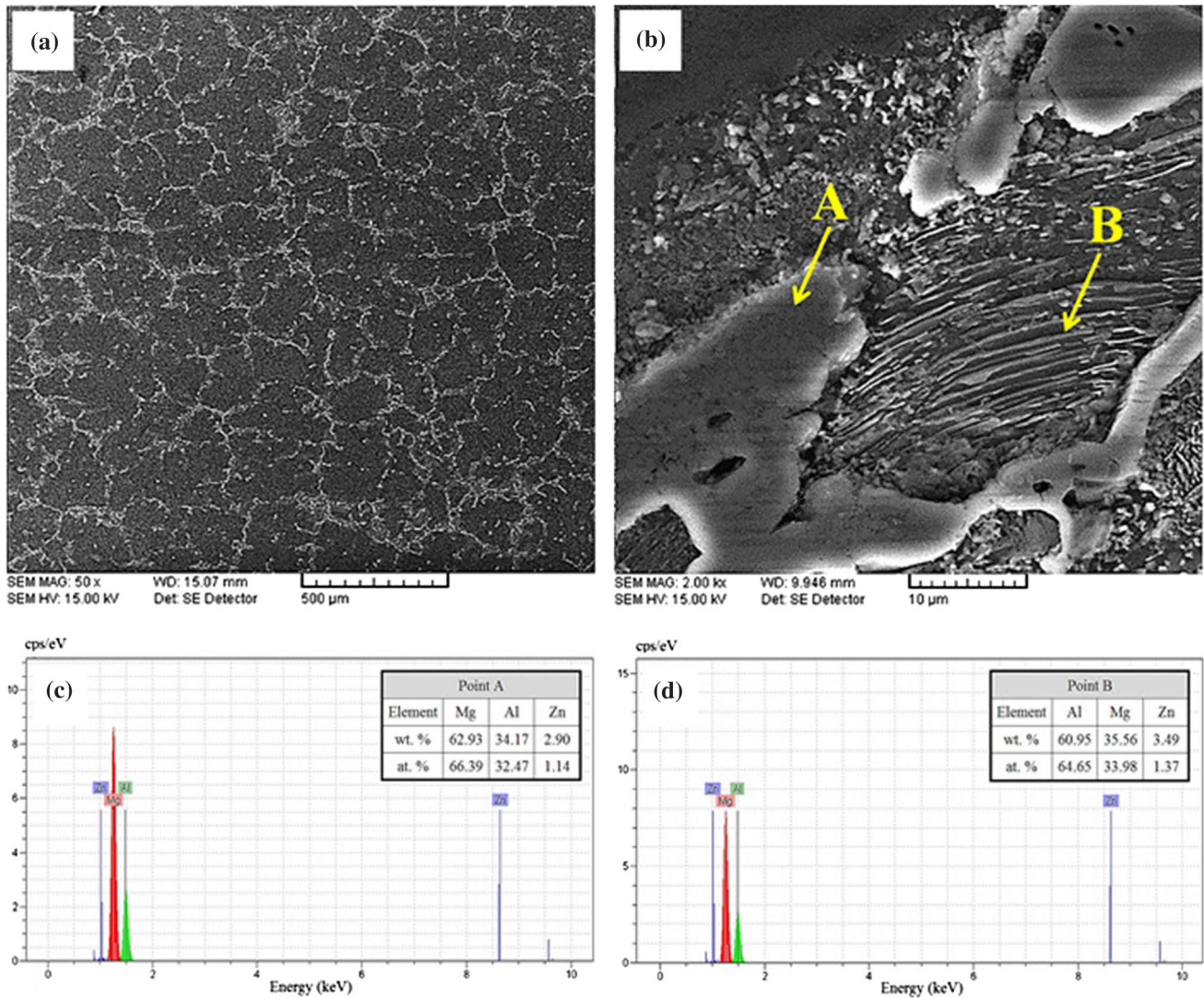


Fig. 2 SEM images of as-cast AZ91 alloy: **a, b** secondary electron image, and **c, d** EDS analysis of the phases shown by A and B, respectively

grain boundaries and the grain size of the alloy has been significantly reduced due to the strain applied in the ECAP process. The grain size distribution is shown in Fig. 4. Measurements showed that the average grain sizes were about 150 μ m in the as-cast condition. According to Fig. 4, the average grain size after ECAP processing is about 14 μ m. After one ECAP pass, the initial coarse grains were divided into many finer grains and create a bimodal structure in the material. Also, the most changes in the grain size occur at this pass because of the high rate of dislocation formation [24–26]. In addition, Homogeneity in grain structure and grain refinement increases with the increase of pass [19, 27, 28]. It is clearly seen that the $\beta(\text{Mg}_{17}\text{Al}_{12})$ intermetallic compounds are broken after ECAP processing. Furthermore, comparing the microstructure of the alloy in as-cast condition (Fig. 2) and after ECAP processing (Fig. 3) indicates that the volume fraction of $\beta(\text{Mg}_{17}\text{Al}_{12})$ phase is reduced

and this phase with lamellar morphology is removed from the microstructure. Considering the Mg–Al phase diagram reveals that the used ECAP temperature (628 K) is about solvus temperature of AZ91 alloy. So, it is estimated that the large portion of $\beta(\text{Mg}_{17}\text{Al}_{12})$ is dissolved in the microstructure as shown in Fig. 3. Similar results have been reported in previous studies for AZ91 alloy processed by equal-channel angular pressing [29–31].

3.2 Creep Properties

Impression creep tests were performed at the temperature range 538–583 K under constant punching stresses in the range 35–95 MPa. Figure 5 typically shows the impression creep curves of ECAPed AZ91 alloy at the temperature range of 538–583 K and a constant temperature of 583 K under normalized stress of 0.00549 and different applied

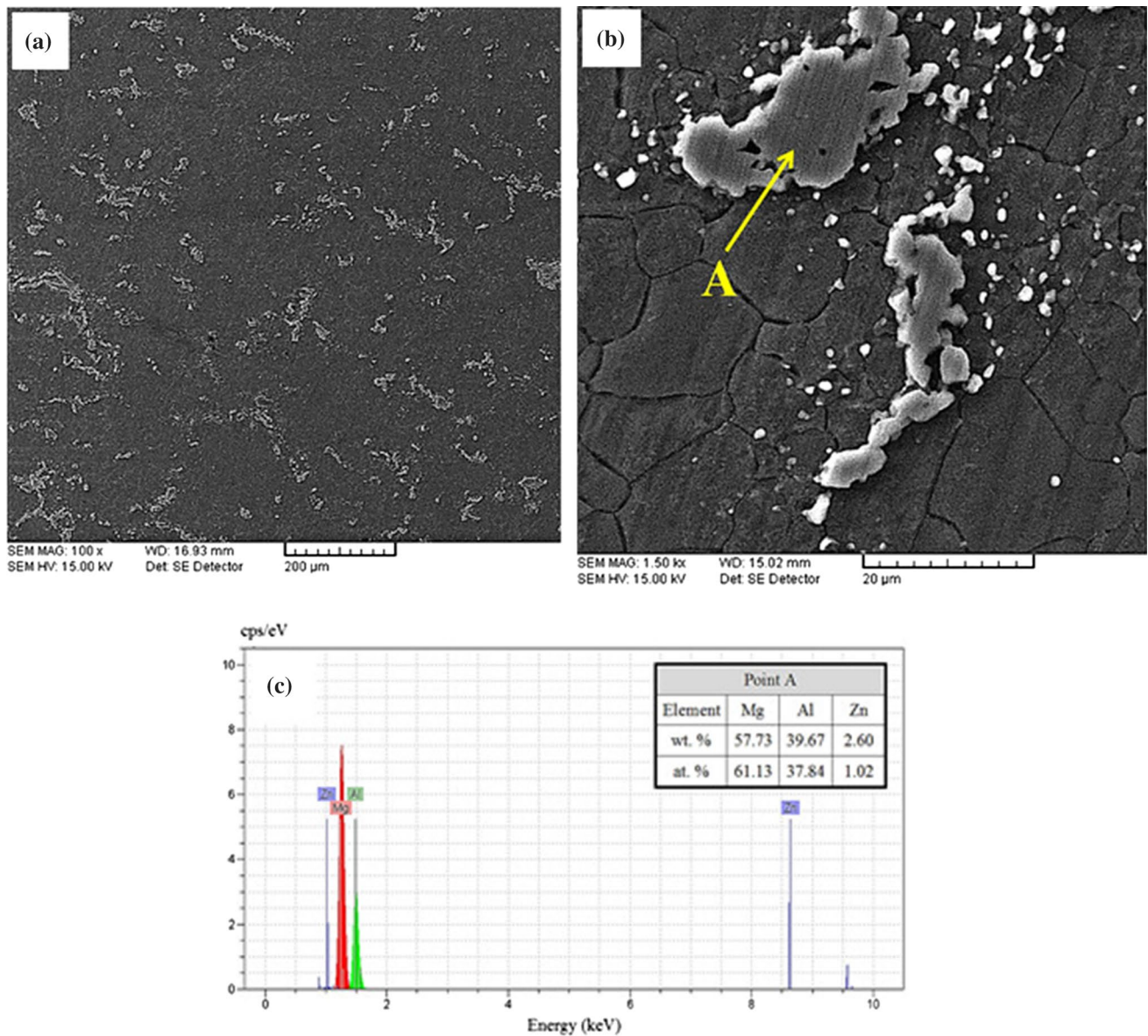


Fig. 3 SEM images of ECAPed AZ91 alloy: **a**, **b** secondary electron image, and **c** EDS analysis of the phase shown by A

stresses, respectively, which are expressed as the variation of punch penetration with creep time. The shear modulus of the alloy was obtained from G (MPa) = 18,460 – 8.2 T (K) [32]. According to this figure, creep curves show that the impression depth increases with increasing both temperature and stress at a specific creep time. Generally, the impression creep curves are composed of the primary and secondary region [33–35]. The creep rate decreases with time in primary creep, but with some types of creep, such as solute drag an inverted primary occurs where the creep rate increases with time [36]. After the primary region, the impression depth increases linearly with time and creep rate remains constant in the secondary or steady state region. The impression rate was computed from the creep curves and has

been plotted in Fig. 6 at the temperature range of 538–583 K and a constant temperature of 583 K under normalized stress of 0.00549 and different applied stresses, respectively. Figures 5 and 6 indicate that the creep curves of the alloy are composed almost of steady state region. Because of the increased dislocation density due to the severe plastic deformation during the ECAP process [28, 37, 38] or the high test temperature, the primary region is significantly reduced and this region is not very evident in the creep curves. Strain hardening is the dominant mechanism in the primary creep stage. So, it is predicted that its rate is decreased with increase dislocation density. However, the primary creep can influence by temperature. The recovery process is pronounced by increasing the test temperature resulting in the

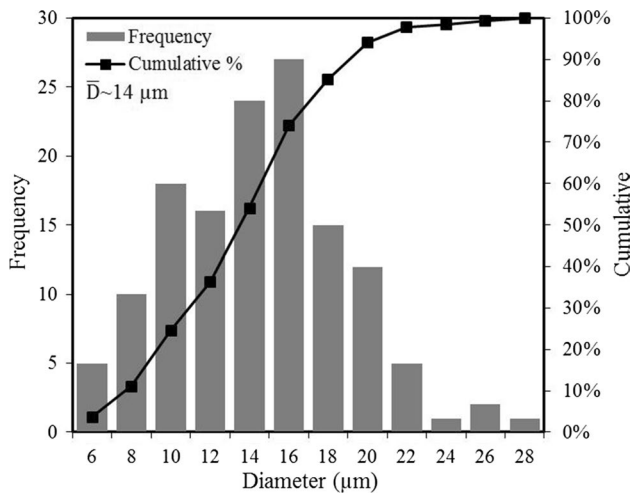


Fig. 4 Grain size distribution for ECAPed alloy

reduced primary creep region as shown in Figs. 5 and 6. A reduction of primary creep for extruded, ECAPed and rolled alloys in previous studies has been reported [39, 40].

The results of previous studies show that the deformation behavior during creep can be determined either by examining microstructure using transmission electron microscope (TEM) or stress exponent and creep activation energy according to the following power-law equation [41–45]:

$$\dot{\epsilon} = A \left(\frac{b}{d}\right)^p \left(\frac{Gb}{kT}\right) \left(\frac{\sigma}{G}\right)^n D \tag{1}$$

where $\dot{\epsilon}$ is the steady-state creep rate, A is the material constant, b is the Burgers vector length (which for Mg is equal to 3.21×10^{-10} m [41]), d is the grain size, p is the grain size exponent, G is the shear modulus, k is Boltzmann’s constant, T is the temperature test in Kelvin, σ is the applied tensile stress, n is the stress exponent ($= 1/m$, where m is the strain-rate sensitivity (SRS) parameter) and D is the diffusion

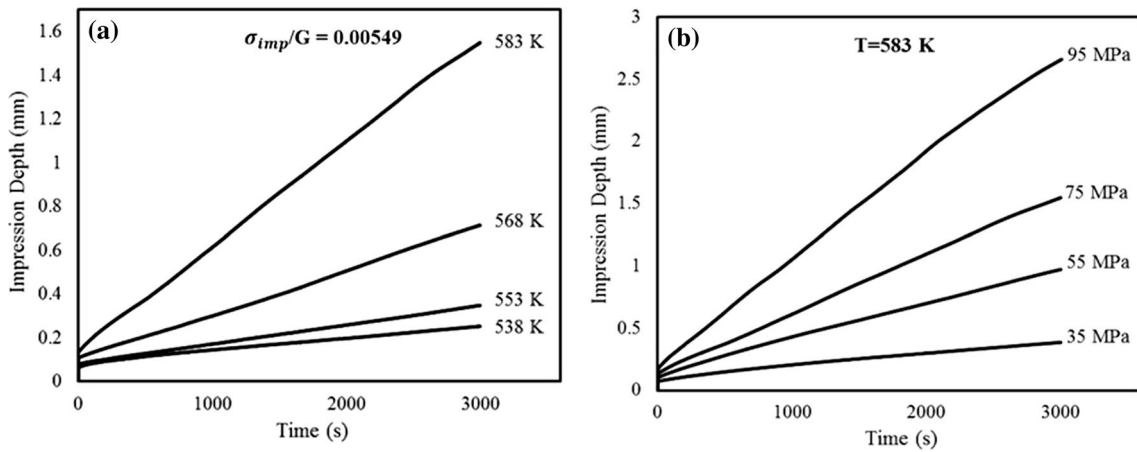


Fig. 5 Impression creep curves obtained from the variation of impression depth versus creep time: **a** at different temperatures under $\sigma_{imp}/G=0.00549$, and **b** at temperature of 583 K under different normalized stresses (σ_{imp}/G)

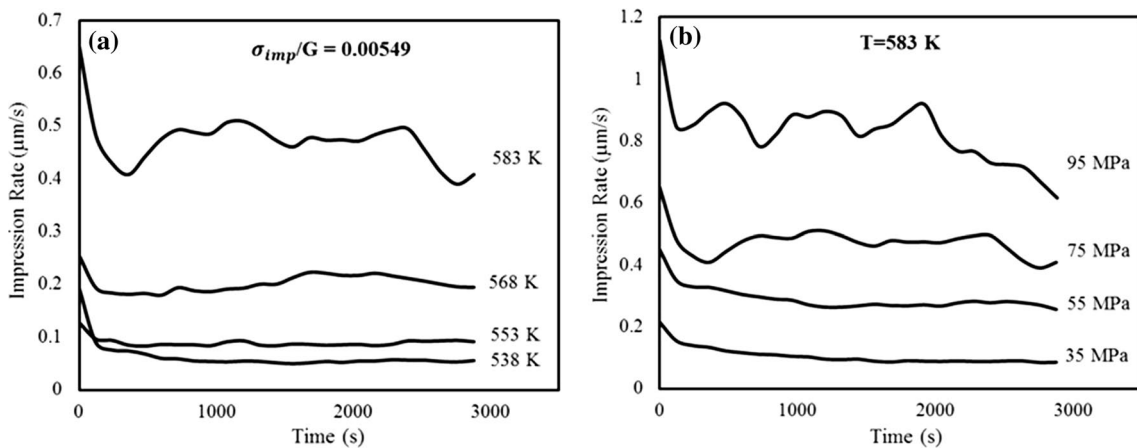


Fig. 6 Variations of impression rate versus creep time: **a** at different temperatures under $\sigma_{imp}/G=0.00549$, and **b** at temperature of 583 K under different normalized stresses (σ_{imp}/G)

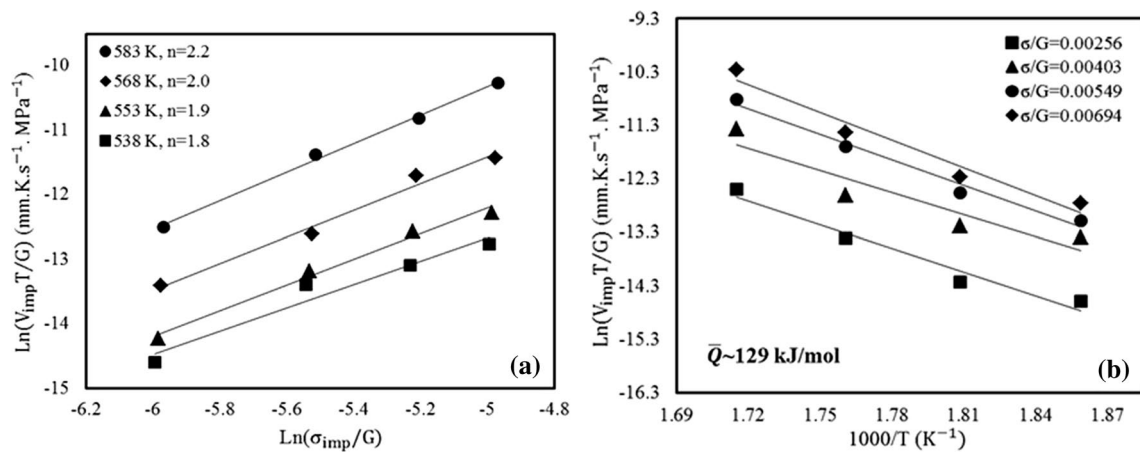


Fig. 7 **a** Variations of $\text{Ln}(V_{\text{imp}}T/G)$ versus $\text{Ln}(\sigma_{\text{imp}}/G)$ at constant temperatures for determining stress exponent, and **b** variations of $\text{Ln}(V_{\text{imp}}T/G)$ versus $1/T$ at constant normalized stresses (σ_{imp}/G) for determining activation energy value

coefficient $[=D_0 \exp(-Q_c/RT)]$, where D_0 is the diffusion constant, Q_c is the activation energy and R is the universal gas constant]. The above equation is used for tensile creep. However, according to the conducted studies on the impression creep method, the following equation was used for the impression creep test [42–46]:

$$\left(\frac{V_{\text{imp}}T}{G}\right) = B \left(\frac{\varphi C_2}{C_1^n}\right) \left(\frac{b}{d}\right)^p \left(\frac{bD_0}{k}\right) \left(\frac{\sigma_{\text{imp}}}{G}\right)^n \exp\left(\frac{-Q_c}{RT}\right) \tag{2}$$

where B , C_1 , and C_2 are constant, V_{imp} is the steady-state impression rate ($=dh/dt$, where h is the impression depth and t is the time), φ is the punch diameter and σ_{imp} is the compressive stress ($=4F/\pi\varphi^2$, where F is load applied to the punch).

For determining the dominant deformation mechanism during creep, it is necessary to calculate the values of stress exponent and activation energy. Using the Eq. 2, the stress exponent, n , and activation energy, Q , can be determined from:

$$n = \left[\frac{\partial \text{Ln}(V_{\text{imp}}T/G)}{\partial \text{Ln}(\sigma_{\text{imp}}/G)} \right]_T \tag{3}$$

$$Q_c = -R \left[\frac{\partial \text{Ln}(V_{\text{imp}}T/G)}{\partial (1/T)} \right]_{(\sigma_{\text{imp}}/G)} \tag{4}$$

According to above equations, the stress exponent and activation energy could be calculated from the slopes of the best-fit line to the variation of $\text{Ln}(V_{\text{imp}}T/G)$ with $\text{Ln}(\sigma_{\text{imp}}/G)$ at constant temperature and $\text{Ln}(V_{\text{imp}}T/G)$ with $1/T$ under constant normalized stress, respectively.

Figure 7a shows the variation of $\text{Ln}(V_{\text{imp}}T/G)$ with $\text{Ln}(\sigma_{\text{imp}}/G)$ at 538, 553, 568, and 583 K for the ECAPed alloy and the slope of lines are shown in the figure. For all temperature, the line slope was close to 2 and the increasing trend of stress exponent with temperature is observed. Considering the obtained values of stress exponent and those reported in the literature [36], the dominant mechanism for this condition is the grain boundary sliding (GBS). Similar deformation mechanism has been reported for AZ91 alloy with grain size about 16 μm at elevated temperature (573 K) [21].

Figure 7b shows the variation of $\text{Ln}(V_{\text{imp}}T/G)$ with $1/T$ under constant normalized stresses. The values of creep activation energy are obtained from the lines which equal to $-Q_c/R$ and shown on the figure. According to this figure, in the constant σ_{imp}/G levels between 0.00256 and 0.00649, the activation energies are close to the activation energy for lattice diffusion in pure magnesium (135 kJ/mol [41]). It has been reported that the creep activation energy in the grain boundary sliding deformation mechanism at $T > 0.6T_m$, where T_m is the absolute melting temperature, is equal to lattice diffusion [17]. Comparing the creep test conditions used in the current study and the grain size with deformation map of AZ series alloys [41], also confirms that the lattice diffusion GBS is the dominant creep mechanism.

3.3 Constitutive Equation

The deformation behavior at the elevated temperatures can be predicted by the constitutive equation. Considering Eqs. 1 and 2, the normalized impression creep rates as a function of normalized stress to the shear modulus are shown in Fig. 8. The creep activation energy was assumed to be equal to the activation energy for lattice diffusion, the grain size exponent, p , was taken as two and $c_1 = 3$ and $c_2 = 1$, as reported

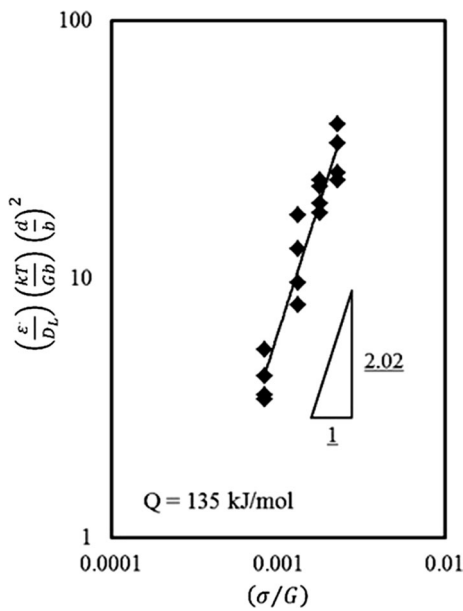


Fig. 8 Variations $(\dot{\varepsilon}/D_L) (kT/Gb) (d/b)^2$ versus (σ/G) in logarithmic axes

in previous studies [23, 36]. The constitutive equation of the alloy was obtained by the best fit of the data points in Fig. 8 as the following equation:

$$\dot{\varepsilon} = 7.25 \left(\frac{b}{d}\right)^2 \left(\frac{Gb}{kT}\right) \left(\frac{\sigma}{G}\right)^{2.02} D_L \quad (5)$$

Using the above equation, the creep properties of AZ91 alloy can be studied where grain boundary sliding is the dominant deformation mechanism.

3.4 Microstructure After Creep

Figure 9 shows the scanning electron microscope image of the alloy after creep testing at different magnifications. According to the previous investigations [22, 23, 47], the microstructure of after-creep specimens in the impression creep test consists of three distinct regions. In region A, which has an approximately hemispherical shape, the stresses are completely hydrostatic and there is no microstructure change. In the region of far from the indenter (region C), the material has no considerable plastic deformation. In region B, which is between regions A and B, $\beta(\text{Mg}_{17}\text{Al}_{12})$ particles have been deformed align to the flow direction of the material. The microstructure in a higher magnification of the deformation zone reveals that elongation in grain has not occurred by plastic deformation. This effect can be attributed to the occurrence of grain boundary sliding mechanism during the creep test. It has been reported that in the deformation zone, the grains are elongated along the direction of the material flow, where dislocation creep is the rate-controlling creep mechanism [22, 23, 47]. The grain size distribution after the creep test in region B is shown in Fig. 10. Comparing Fig. 4 with Fig. 10 reveals that the grain size has remained constant after the creep test. So, it can say that recrystallization and grain growth have not taken place during the creep test.

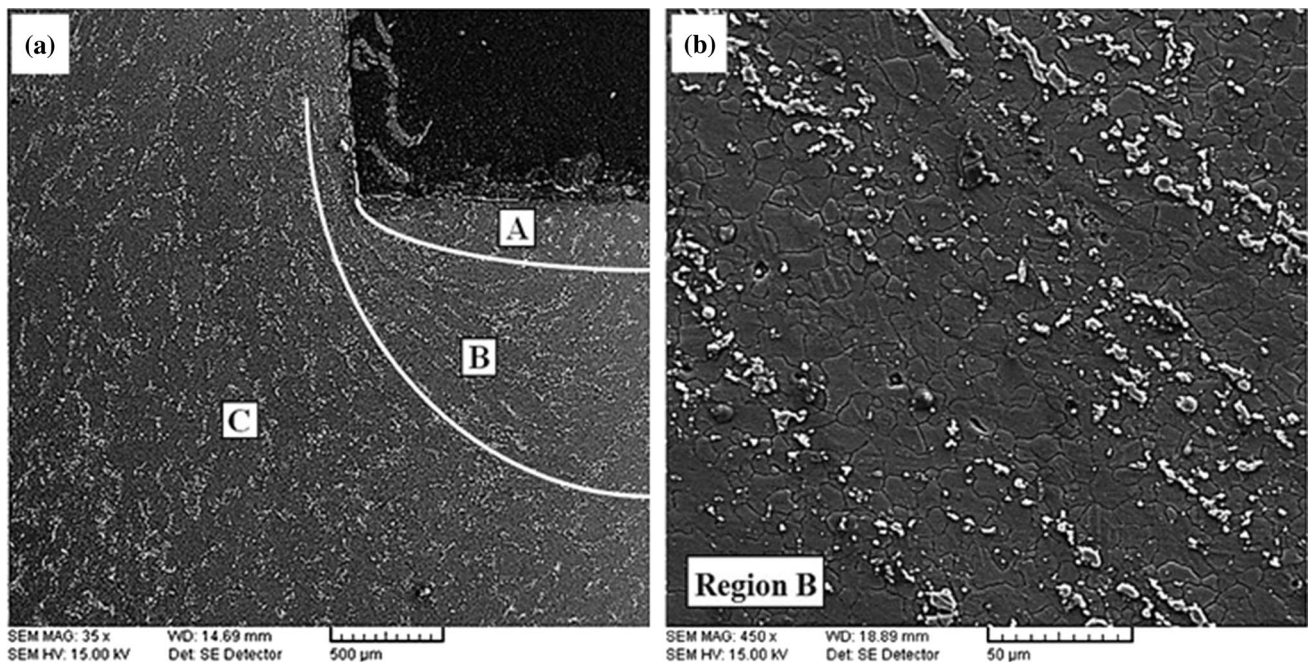


Fig. 9 Microstructure of the alloy after creep test at temperature of 568 K under $\sigma_{\text{imp}}/G=0.00694$ for 3000 s: **a** beneath the indenter, and **b** region B

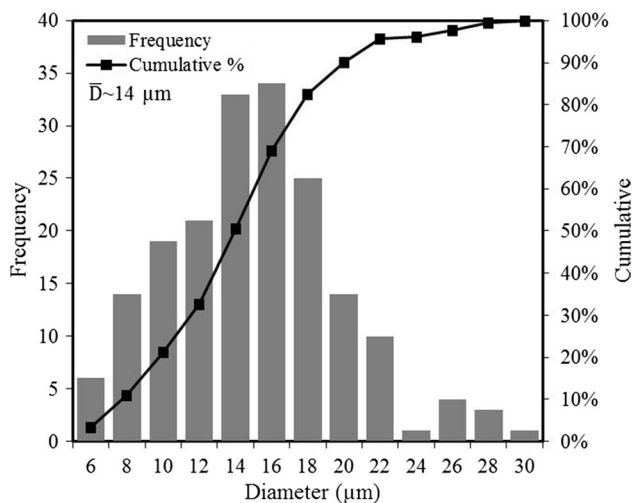


Fig. 10 Grain size distribution after the creep test in region B

4 Summary and Conclusions

The effect of severe plastic deformation at high temperature on the microstructure and creep properties of the AZ91 magnesium alloy was studied. Microstructural evolution revealed that the structure of the AZ91 alloy in casting condition consists of $\beta(\text{Mg}_{17}\text{Al}_{12})$ intermetallic phase in $\alpha(\text{Mg})$ matrix with lamellar and massive morphologies. After four-step ECAP processing at the temperature of 628 K, the volume fraction of $\beta(\text{Mg}_{17}\text{Al}_{12})$ phase decreased and this phase with lamellar morphology was removed from the microstructure of the alloy. Also, an ultrafine-grained microstructure with an average grain size of about 14 μm was produced from the initial coarse grained structure in the as-cast material. Creep properties of AZ91 magnesium alloy After four-step ECAP processing at the temperature of 628 K were investigated using the impression creep technique at the temperature range of 538–583 K under shear modulus normalized stress between 0.00256 and 0.00694. Based on the power-law equation, the stress exponent was in the range of 1.8 to 2.2 and the activation energy of creep was about 129 kJ/mol. The calculated creep parameters and microstructural evolution reveal that the operative deformation mechanism is grain boundary sliding during creep at low stresses and high temperatures.

References

- X.U. Yan, L.X. Hu, S.U.N. Yu, J.B. Jia, J.F. Jiang, *Trans. Nonferrous Met. Soc. China* **25**, 381 (2015)
- X.C. Luo, D.T. Zhang, W.W. Zhang, C. Qiu, D.L. Chen, *Mater. Sci. Eng., A* **725**, 398 (2018)
- G. Zeng, C. Liu, Y. Wan, Y. Gao, S. Jiang, Z. Chen, *Mater. Sci. Eng., A* **734**, 59 (2018)
- B.L. Mordike, T. Ebert, *Mater. Sci. Eng., A* **302**, 37 (2001)
- M. Celikin, M. Pegguleryuz, in *TMS Annual Meeting & Exhibition* (Springer, Cham, 2018), p. 337
- D.H. Hou, S.M. Liang, R.S. Chen, C. Dong, E.H. Han, *Acta Metall. Sin. (Engl. Lett.)* **28**, 115 (2015)
- B.A. Esgandari, H. Mehrjoo, B. Nami, S.M. Miresmaeili, *Mater. Sci. Eng., A* **528**, 5018 (2011)
- R. Panicker, A.H. Chokshi, R.K. Mishra, R. Verma, P.E. Krajewski, *Acta Mater.* **57**, 3683 (2009)
- J. Xu, X. Wang, X. Zhu, M. Shirooyeh, J. Wongsangam, D. Shan, B. Guo, T.G. Langdon, *J. Mater. Sci.* **48**, 4117 (2013)
- Y. Yuan, A. Ma, X. Gou, J. Jiang, G. Arhin, D. Song, H. Liu, *Mater. Sci. Eng., A* **677**, 125 (2016)
- R.Z. Valiev, Y. Estrin, Z. Horita, T.G. Langdon, M.J. Zechetbauer, Y.T. Zhu, *JOM* **58**, 33 (2006)
- T.G. Langdon, *Mater. Sci. Eng., A* **462**, 3 (2007)
- R.Z. Valiev, T.G. Langdon, *Prog. Mater. Sci.* **51**, 881 (2006)
- A. Yamashita, D. Yamaguchi, Z. Horita, T.G. Langdon, *Mater. Sci. Eng., A* **287**, 100 (2000)
- R.B. Figueiredo, T.G. Langdon, *J. Mater. Sci.* **43**, 7366 (2008)
- P.S. Roodposhti, A. Sarkar, K.L. Murty, H. Brody, R. Scattergood, *Mater. Sci. Eng., A* **669**, 171 (2016)
- M. Alvarez-Leal, A. Orozco-Caballero, F. Carreno, O.A. Ruano, *Mater. Sci. Eng., A* **710**, 240 (2018)
- Y.H. Wei, Q.D. Wang, Y.P. Zhu, H.T. Zhou, W.J. Ding, Y. Chino, M. Mabuchi, *Mater. Sci. Eng., A* **360**, 107 (2003)
- R.B. Figueiredo, T.G. Langdon, *Mater. Sci. Eng., A* **501**, 105 (2009)
- L. Li, W. Wei, Y. Lin, C. Lijia, L. Zheng, *J. Mater. Sci.* **41**, 409 (2006)
- K. Kubota, M. Mabuchi, K. Higashi, *J. Mater. Sci.* **34**, 2255 (1999)
- B. Nami, H. Razavi, S. Mirdamadi, S.G. Shabestari, S.M. Miresmaeili, *Metall. Mater. Trans. A* **41**, 1973 (2010)
- F. Kabirian, R. Mahmudi, *Metall. Mater. Trans. A* **40**, 116 (2009)
- R. Jahadi, M. Sedighi, H. Jahed, *Mater. Sci. Eng., A* **593**, 178 (2014)
- S.H. Kang, Y.S. Lee, J.H. Lee, *J. Mater. Process. Technol.* **201**, 436 (2008)
- K.R. Gopi, H.S. Nayaka, S. Sahu, *J. Mater. Eng. Perform.* **26**, 3399–3409 (2017)
- S.B. Xu, Q.I.N. Zhen, L.I.U. Ting, C.N. Jing, G.C. Ren, *Trans. Nonferrous Met. Soc. China* **22**, 61 (2012)
- X.M. Feng, T.T. Ai, *Trans. Nonferrous Met. Soc. China* **19**, 293–298 (2009)
- C.W. Chung, R.G. Ding, Y.L. Chiu, W. Gao, *J. Phys: Conf. Ser.* **241**, 012101 (2010)
- Y. Yuan, A. Ma, J. Jiang, F. Lu, W. Jian, D. Song, Y.T. Zhu, *Mater. Sci. Eng., A* **588**, 329 (2013)
- B. Chen, D.L. Lin, L. Jin, X.Q. Zeng, C. Lu, *Mater. Sci. Eng., A* **483**, 113 (2008)
- K. Ishikawa, H. Watanabe, T. Mukai, *Mater. Lett.* **59**, 1511 (2005)
- F. Yang, J.C. Li, *Mater. Sci. Eng., R* **74**, 233 (2013)
- E.M. Mazraeshahi, B. Nami, S.M. Miresmaeili, *Mater. Des.* **51**, 427 (2013)
- R.J. Nabariya, S. Goyal, M. Vasudevan, N. Arivazhagan, *Mater. Today Proc.* **5**, 12320 (2018)
- M.E. Kassner, M.T. Perez-Prado, *Fundamentals of Creep in Metals and Alloys*, 1st edn. (Elsevier Science, Amsterdam, 2004)
- A. Heczal, F. Akbaripanah, M.A. Salevati, R. Mahmudi, A. Vida, J. Gubicza, *J. Alloys Compd.* **763**, 629 (2018)
- M. Janeček, J. Čížek, J. Gubicza, J. Vrátná, *J. Mater. Sci.* **47**, 7860 (2012)
- J.N. Wang, A.J. Schwartz, T.G. Nieh, D. Clemens, *Mater. Sci. Eng., A* **206**, 63 (1996)
- R. Mahmudi, R. Alizadeh, A.R. Geranmayeh, *Scr. Mater.* **64**, 521 (2011)

41. H. Somekawa, K. Hirai, H. Watanabe, Y. Takigawa, K. Higashi, *Mater. Sci. Eng. A* **407**, 53 (2005)
42. S.M. Miresmaeili, B. Nami, *Mater. Des.* **56**, 286 (2014)
43. B. Kondori, R. Mahmudi, *Mater. Sci. Eng., A* **700**, 438 (2017)
44. S.N.G. Chu, J.C.M. Li, *J. Mater. Sci.* **12**, 2200 (1977)
45. J.C. Li, *Mater. Sci. Eng., A* **322**, 23 (2002)
46. S.M. Miresmaeili, B. Nami, R. Abbasi, I. Khoubrou, *JOM* **71**, 2128–2135 (2019)
47. S. Ganguly, A.K. Mondal, *Mater. Sci. Eng., A* **718**, 377 (2018)

Publisher's Note Springer Nature remains neutral with regard to jurisdictional claims in published maps and institutional affiliations.